Real-Time Corrosion Monitoring of Aircraft Structures with Prognostic Applications

Douglas Brown[1], Duane Darr[2], Jefferey Morse[3], and Bernard Laskowski[4]

[1,2,3,4] *Analatom, Inc., 562 E. Weddell Dr. Suite 4, Sunnyvale, CA 94089-2108, USA*
Doug.Brown@analatom.com
Duane.Darr@analatom.com
Jeff.Morse@analatom.com
Bernard.Laskowski@analatom.com

ABSTRACT

This paper presents the theory and experimental validation of a Structural Health Management (SHM) system for monitoring corrosion. Corrosion measurements are acquired using a micro-sized Linear Polarization Resistance (μLPR) sensor. The μLPR sensor is based on conventional macro-sized Linear Polarization Resistance (LPR) sensors with the additional benefit of a reduced form factor making it a viable and economical candidate for remote corrosion monitoring of high value structures, such as buildings, bridges, or aircraft.

A series of experiments were conducted to evaluate the μLPR sensor for AA 7075-T6, a common alloy used in aircraft structures. Twelve corrosion coupons were placed alongside twenty-four μLPR sensors in a series of accelerated tests. LPR measurements were sampled once per minute and converted to a corrosion rate using the algorithms presented in this paper. At the end of the experiment, pit-depth due to corrosion was computed from each μLPR sensor and compared with the control coupons.

The paper concludes with a feasibility study for the μLPR sensor in prognostic applications. Simultaneous evaluation of twenty-four μLPR sensors provided a stochastic data set appropriate for prognostics. RUL estimates were computed a-posteriori for three separate failure thresholds. The results demonstrate the effectiveness of the sensor as an efficient and practical approach to measuring pit-depth for aircraft structures, such as AA 7075-T6, and provide feasibility for its use in prognostic applications.

1. INTRODUCTION

Recent studies have exposed the generally poor state of our nation's critical infrastructure systems that has resulted from wear and tear under excessive operational loads and environmental conditions. SHM (Structural Health Monitoring) Systems aim at reducing the cost of maintaining high value structures by moving from SBM (Scheduled Based Maintenance) to CBM (Condition Based Maintenance) schemes (Huston, 2010). These systems must be low-cost, simple to install with a user interface designed to be easy to operate. To reduce the cost and complexity of such a system a generic interface node that uses low-powered wireless communications has been developed. This node can communicate with a myriad of common sensors used in SHM. In this manner a structure such as a bridge, aircraft or ship can be fitted with sensors in any desired or designated location and format without the need for communications and power lines that are inherently expensive and complex to route. Data from these nodes is transmitted to a central communications Personal Computer (PC) for data analysis. An example of this is provided in Figure 1 showing an embedded SHM system installed in the rear fuel-bay bulkhead of a commercial aircraft.

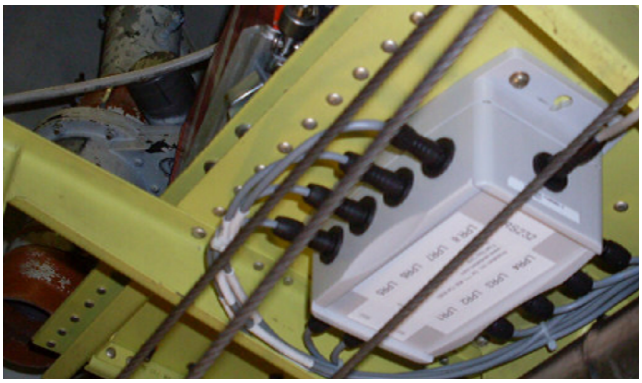

Figure 1. Embedded SHM system installed in the rear fuel-bay bulkhead of a commercial aircraft.

Corrosion sensors can be distinguished by the following categories, *direct* or *indirect* and *intrusive* or *non-intrusive*. Direct corrosion monitoring measures a response signal, such

as a current or voltage, as direct result of corrosion. Examples of common direct corrosion monitoring techniques are: corrosion coupons, Electrical Resistance (ER), Electro-Impedance Spectroscopy (EIS) and Linear Polarization Resistance (LPR) techniques. Whereas, indirect corrosion monitoring techniques measure an outcome of the corrosion process. Two of the most common indirect techniques are ultrasonic testing and radiography. An intrusive measurement requires access to the structure. Corrosion coupons, ER, EIS and LPR probes are intrusive since they have to access the structure. Non-intrusive techniques include ultrasonic testing and radiography.

Each of these methods have advantages and disadvantages. Corrosion coupons provide the most reliable physical evidence possible. Unfortunately, coupons usually require significant time in terms of labor and they provide time averaged data that can not be utilized for real time or on-line corrosion monitoring (Harris, Mishon, & Hebbron, 2006). ER probes provide a basic measurement of metal loss, but unlike coupons, the value of metal loss can be measured at any time, as frequently as required, while the probe is in-situ and permanently exposed to the structure. The disadvantage is ER probes require calibration with material properties of the structure to be monitored. The advantage of the LPR technique is that the measurement of corrosion rate is made instantaneously. This is a more powerful tool than either coupons or ER where the fundamental measurement is metal loss and where some period of exposure is required to determine corrosion rate. The disadvantage to the LPR technique is that it can only be successfully performed in relatively clean aqueous electrolytic environments (*Introduction to Corrosion Monitoring*, 2012). EIS is a very powerful technique that provides both kinetic (corrosion rate) and mechanistic information. The main disadvantages associated with the use of EIS are that the instrumentation is sophisticated and sometimes difficult to use in the field due to the length of time required for each frequency sweep. Additionally, interpretation of the data can be difficult (Buchheit, Hinkebein, Maestas, & Montes, 1998). Finally, ultrasonic testing and radiography can be used to detect and measure (depth) of corrosion through non-destructive and non-intrusive means (Twomey, 1997). The disadvantage with the ultrasonic testing and radiography equipment is the same with corrosion coupons, both require significant time in terms of labor and can not be utilized for real time or on-line corrosion monitoring.

The μLPR presented in this paper improves on existing LPR technology by reducing the form-factor of the sensor to the size of a United States postage stamp, shown in Figure 2, to enable real-time sensing of remote and hard-to-access areas where conventional sensors cannot due to limitations in size and form-factor. Further improvements are realized by narrowing the separation distance between electrodes, which

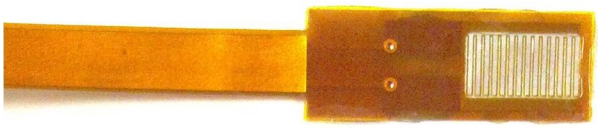

(a)

(b)

Figure 2. One-to-one scaled comparison of (a) the μLPR sensor attached to a flexcable and (b) a United States postage stamp.

minimizing the effects due to solution resistance. This enables the μLPR to operate outside a controlled aqueous environment, such as an electro-chemical cell, in a broad range of fielded applications (eg. civil engineering, aerospace, petrochemical).

The remainder of the paper is organized by the following. Section 2 describes the general theory governing LPR. Section 3 presents the μLPR discussing the benefits of miniaturizing the sensor from a macro-scaled LPR. Section 4 outlines the experimental setup and procedure used to validate the μLPR sensor. Section 5 presents the experimental measurements with the accompanying analysis which demonstrates the effectiveness of the μLPR sensor. Section 6 evaluates the feasibility for using the μLPR sensor in prognostic applications. Finally, the paper is concluded in Section 7 with a summary of the findings and future work.

2. LPR THEORY

The corrosion of metals takes place when the metal dissolves due to oxidation and reduction (electrochemical) reactions at the interface of metal and the (aqueous) electrolyte solution. Atmospheric water vapor is an example of an electrolyte that corrodes exposed metal surface and wet concrete is another example of an electrolyte that can cause corrosion of reinforced rods in bridges. Corrosion usually proceeds through a combination of electrochemical reactions; (1) anodic (oxidation) reactions involving dissolution of metals in the electrolyte and release of electrons, and (2) cathodic (reduction) reactions involving gain of electrons by the electrolyte species like atmospheric oxygen O_2, moisture H_2O, or H+ ions in an acid (Bockris, Reddy, & Gambola-Aldeco, 2000). The flow of electrons from the anodic reaction sites to the cathodic reaction sites constitutes corrosion current and is used to estimate the corrosion rate. When the two reactions are in equilibrium at the equilibrium corrosion poten-

tial, E_{corr}, the net current on the metal surface is zero without an external source of current. The anodic reactions proceed more rapidly at more positive potentials and the cathodic reactions proceed more rapidly at more negative potentials. Since the corrosion current from the unstable anodic and cathodic sites is too small to measure, an external activation potential is applied across the metal surface and the current is measured for electrochemical calculations. The resulting E_a vs. I_a curve is called the polarization curve. Under external activation potential, the anodic and cathodic currents increase exponentially and so when $\log_{10} I_a$ is plotted against E_a (a Tafel Plot), the linear regions on the anodic and cathodic curves correspond to regions where either the anodic or cathodic reactions dominate and represent the rate of the electrochemical process. The extrapolation of the Tafel linear regions to the corrosion potential gives the corrosion current, I_{corr}, which is then used to calculate the rate of corrosion (Burstein, 2005).

2.1. Anodic and Cathodic Reactions

Electrochemical technique of Linear Polarization Resistance (LPR) is used to study corrosion processes since the corrosion reactions are electrochemical reactions occurring on the metal surface. Modern corrosion studies are based on the concept of mixed potential theory postulated by Wagner and Traud, which states that the net corrosion reaction is the result of two or more partial electrochemical reactions that proceed independently of each other (Wagner & Traud, 1938). For the case of metallic corrosion in presence of an aqueous medium, the corrosion process can be written as,

$$\mathrm{M} + z\mathrm{H_2O} \underset{b}{\overset{f}{\longleftrightarrow}} \mathrm{M}^{z+} + \frac{z}{2}\mathrm{H_2} + z\mathrm{OH}^-, \tag{1}$$

where z is the number of electrons lost per atom of the metal. This reaction is the result of an anodic (oxidation) reaction,

$$\mathrm{M} \underset{b}{\overset{f}{\longleftrightarrow}} \mathrm{M}^{z+} + ze^-, \tag{2}$$

and a cathodic (reduction) reaction,

$$z\mathrm{H_2O} + ze^- \underset{b}{\overset{f}{\longleftrightarrow}} \frac{z}{2}\mathrm{H_2} + z\mathrm{OH}^-. \tag{3}$$

It is assumed that the anodic and cathodic reactions occur at a number of sites on a metal surface and that these sites change in a dynamic statistical distribution with respect to location and time. Thus, during corrosion of a metal surface, metal ions are formed at anodic sites with the loss of electrons and these electrons are then consumed by water molecules to form hydrogen molecules. The interaction between the anodic and cathodic sites as described on the basis of mixed potential theory is represented by well-known relationships using current (reaction rate) and potential (driving force). For the above pair of electrochemical reactions (anodic (2) and cathodic (3)), the relationship between the applied current I_a and potential E_a follows the Butler-Volmer equation,

$$I_a = I_{corr}\left\{\exp\left[\frac{2.303\,(E_a - E_{corr})}{\beta_a}\right] - \ldots \right. \\ \left. \exp\left[-\frac{2.303\,(E_a - E_{corr})}{\beta_c}\right]\right\}, \tag{4}$$

where β_a and β_c are the anodic and cathodic Tafel parameters given by the slopes of the polarization curves $\partial E_a/\partial \log_{10} I_a$ in the anodic and cathodic Tafel regimes, respectively and E_{corr} is the corrosion potential (Bockris et al., 2000).

2.2. Electrode Configuration

An electrode is a (semi-)conductive solid that interfaces with an electrolytic solution. The most common electrode configuration is the three-electrode configuration. The common designations are: working, reference and counter electrodes. The working electrode is the designation for the electrode being studied. In corrosion experiments, this is the material that is corroding. The counter electrode is the electrode that completes the current path. All electrochemistry experiments contain a working–counter pair. In most experiments the counter electrode is simply the current source/sink comprised of inert materials like graphite or platinum. Finally, the reference electrode serves as an experimental reference point, specifically for potential (sense) measurements. The reference electrode is positioned so that it measures a point very close to the working electrode.

The three-electrode setup has a distinct experimental advantage over a two electrode setup: only one half of the cell is measured. That is, potential changes of the working electrode are measured independently of changes that may occur at the counter electrode. This configuration also reduces the effect of measuring potential drops across the solution resistance when measuring between the working and counter electrodes.

2.3. Polarization Resistance

The corrosion current, I_{corr}, cannot be measured directly. However, a-priori knowledge of β_a and β_c along with a small signal analysis technique, known as polarization resistance, can be used to indirectly compute I_{corr}. The polarization resistance technique, also referred to as "linear polarization", is an experimental electrochemical technique that estimates the small signal changes in I_a when E_a is perturbed by $E_{corr} \pm 10\,\mathrm{mV}$ (G102, 1994). The slope of the resulting curve over this range is the polarization resistance,

$$R_p \triangleq \left.\frac{\partial E_a}{\partial I_a}\right|_{|E_a - E_{corr}| \le 10\,\mathrm{mV}}. \tag{5}$$

Note, the applied current, I_a, is the total applied current and is not multiplied by the electrode area so R_p as defined in (5)

has units of Ω. Provided that $|E_a - E_{corr}|/\beta_a \leq 0.1$ and $|E_a - E_{corr}|/\beta_c \leq 0.1$, the first order Taylor series expansion $\exp(x) \approxeq 1 + x$ can be applied to (4) and (5) to arrive at,

$$R_p = \frac{1}{2.303 I_{corr}} \left(\frac{\beta_a \beta_c}{\beta_a + \beta_c} \right). \quad (6)$$

Finally, this expression can be re-written for I_{corr} to arrive at the Stern-Geary equation,

$$I_{corr} = \frac{B}{R_p}, \quad (7)$$

where $B = \frac{1}{2.303} [\beta_a \beta_c / (\beta_a + \beta_c)]$ is a constant of proportionality.

2.4. Pit-Depth

The pit-depth due to corrosion is calculated by computing the pitting current density, i_{pit},

$$i_{pit}(t) = \frac{i_{corr} - i_{pv}}{N_{pit}}, \quad (8)$$

where $i_{corr} = I_{corr}/A_{sen}$ is the corrosion current density, i_{pv} is the passive current density, N_{pit} is the pit density for the alloy (derived empirically) and A_{sen} is the effective surface area of the LPR sensor. One critical assumption is the pH is in the range of 6-8. If this cannot be assumed, then a measurement of pH is required and $i_{passive}$ is needed over the range of pH values. Next, Faraday's law is used to relate the total pitting charge with respect to molar mass loss. Let the equivalent weight (EW) represent the weight of the metal that reacts with $1\,\mathrm{C}$ of charge, thus contributing to the corrosion and overall loss of material in the anodic (oxidation) reaction given in (2). The total pitting charge, Q_{corr}, and molar mass loss, M, can be related to the following,

$$Q_{pit}(t) = zF \cdot M(t), \quad (9)$$

where $F = 9.650 \times 10^4\,\mathrm{C/mol}$ is Faraday's constant, and z is the number of electrons lost per atom in the metal in the reduction-oxidation reaction. The EW is calculated from the known Atomic Weight (AW) of the metal,

$$EW = \frac{AW}{z}. \quad (10)$$

Next, the number of moles of the metal reacting can be converted to an equivalent mass loss, m_{loss},

$$m_{loss}(t) = M(t) \cdot AW. \quad (11)$$

Combining (9) through (11), the mass loss m_{loss} is related to Q_{pit} by,

$$m_{loss}(t) = \frac{EW \cdot Q_{pit}(t)}{F}. \quad (12)$$

With the mass loss calculated and knowing the density ρ, the pit-depth modeled using a semi-spherical volume with a depth (or radius) d is expressed as,

$$d(t) = \left(\frac{3 m_{loss}(t)}{2\pi\rho} \right)^{1/3}. \quad (13)$$

Now, note that Q_{pit} can be found by integrating i_{pit} over the total time,

$$Q_{pit}(t) = \int_0^t i_{pit}(\tau)\, d\tau, \quad (14)$$

Substituting (12) and (14) into (13) gives,

$$d(t) = \sqrt[3]{\frac{3EW}{2\pi\rho F} \int_0^t i_{pit}(\tau)\, d\tau}. \quad (15)$$

Next, by substituting (7) and (8) into (15), the expression for d can be rewritten as,

$$d(t) = \sqrt[3]{\frac{3EW}{2\pi\rho N_{pit} F} \int_0^t \left(\frac{B}{A_{sen} R_p(\tau)} - i_{pv} \right) d\tau}. \quad (16)$$

In practice, R_p is not measured continuously, rather, periodic measurements are taken every T_s seconds. If its assumed over this interval the R_p values changes linearly then the mean value theorem for integrals can be applied to arrive at an alternative expression for d,

$$d(t) = \sqrt[3]{\frac{3T_s EW}{2\pi\rho N_{pit} F} \sum_{k=0}^{N-1} \left(\frac{B}{A_{sen} R_p(kT_s)} - i_{pv} \right)}. \quad (17)$$

2.5. Standard Measurements

2.5.1. Polarization Resistance

ASTM standard G59 outlines procedures for measuring polarization resistance. Potentiodynamic, potential step, and current-step methods can be used to compute R_p (G59, 1994). The potentiodynamic sweep method is the most common method for measuring R_p. A potentiodynamic sweep is conducted by applying E_a between $E_{corr} \pm 10\,\mathrm{mV}$ at a slow scan rate, typically $0.125\,\mathrm{mV/s}$. A linear fit of the resulting E_a vs. I_a curve is used to compute R_p.

2.5.2. Tafel Coefficients

ASTM standard G59 outlines the procedure for measuring the Tafel slopes, β_a and β_c (G59, 1994). First, E_{corr} is measured from the open circuit potential. Next, E_a is initialized to $E_{corr} - 250\,\mathrm{mV}$. Then, a potentiodynamic sweep is conducted by increasing E_a from $E_{corr} - 250\,\mathrm{mV}$ to $E_{corr} + 250\,\mathrm{mV}$ at a slow scan rate, typically $0.125\,\mathrm{mV/s}$. Next, a Tafel curve is plotted for E_a vs $\log_{10} I_a$ as illustrated by the example in Figure 3. Values for β_a and β_c are estimated from the slopes of the linear extrapolated anodic and cathodic currents, which are identified in Figure 3.

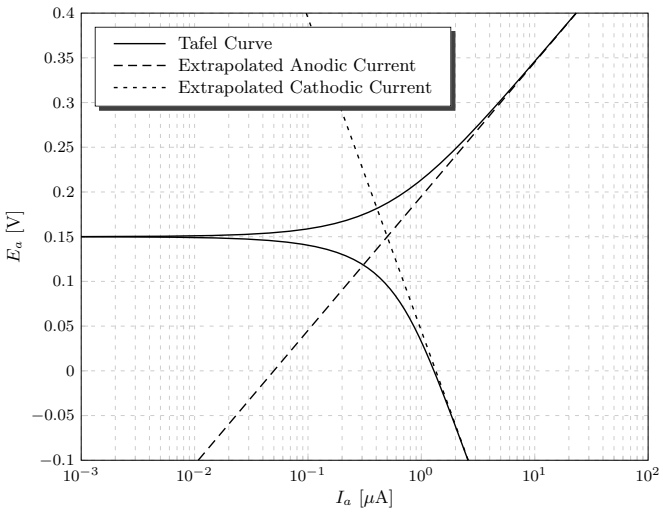

Figure 3. Illustration of a typical Tafel curve identifying the extrapolated anodic and cathodic currents.

3. μLPR Corrosion Sensor

In this section, a micro-LPR (μLPR) is presented which uses the potential step-sweep method to compute polarization resistance. The μLPR works on the same principle as the macro-sized LPR sensors and is designed to corrode at the same rate as the structure on which it is placed. Although LPR theory is well established and accepted as a viable corrosion monitoring technique, conventional macro-sized LPR sensor systems are expensive and highly intrusive. The μLPR is a micro-scaled LPR sensor inspired from the macro-sized version discussed in the previous section. Scaling the LPR sensor into a micro-sized package provides several advantages which include,

- Miniature form factor
- Two-pair electrode configuration
- Faster LPR measurements

3.1. Form Factor

Expertise in semiconductor manufacturing is used to micromachine the μLPR. Using photolithography it is possible to manufacture the μLPR sensor from a variety of standard engineering construction materials varying from steels for buildings and bridges through to novel alloys for airframes. The micro sensor is made up of two micro machined electrodes that are interdigitated at $150\,\mu\mathrm{m}$ spacing. The μLPR sensor is made from shim stock of the source/sample material that is pressure and thermally bonded to Kapton tape. The shim is prepared using photolithographic techniques and Electro Chemical Etching (ECM). It is further machined on the Kapton to produce a highly ductile and mechanically robust micro sensor that is very sensitive to corrosion. Images of the μLPR shown bare and a fitted sensor underneath a coating are shown in Figure 4.

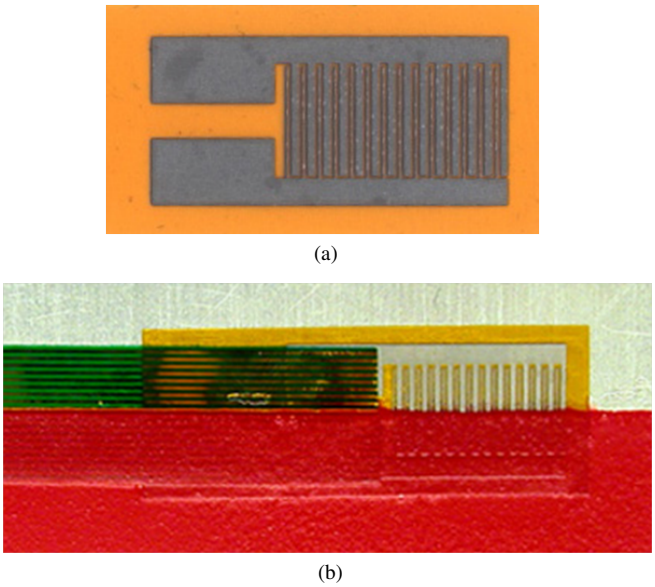

(a)

(b)

Figure 4. Thin film μLPR sensor (a) exposed and (b) quasi-exposed with the lower-half underneath a coating.

3.2. Electrode Configuration

The μLPR differs from conventional macro-sized LPR sensors in two major ways. First, the μLPR is a two electrode device. The reference electrode is eliminated as the separation distance between the working and counter electrodes, typically $150\,\mu\mathrm{m}$, minimizes any voltage drop due to the solution resistance, R_s. Second, both electrodes are composed of the same working metal. This is uncommon in most electrochemical cells where the counter electrode is made of an inert material. The benefit is the electrodes provide a more direct measurement of corrosion than techniques which use electrodes made of different metals (eg. gold).

3.3. LPR Measurements

Potential step-sweeps are performed by applying a series of 30 steps over a range of $\pm 10\,\mathrm{mV}$ spanning a period of $2.6\,\mathrm{s}$. This allows eight μLPR sensors to be measured in less than $30\,\mathrm{s}$. However, the effective scan-rate of $7.7\,\mathrm{mV/s}$ generates an additional current, I_{dl}, due to rapid charging and discharging of the capacitance, referred to as the double-layer capacitance C_{dl}, at the electrode-electrolyte interface,

$$I_{dl} = C_{dl}\frac{dE_a}{dt}. \tag{18}$$

Let the resulting polarization resistance that is computed when I_{dl} is non-zero be represented by $\hat{R}_p$. It can be shown that $\hat{R}_p$ is related to R_p by the following,

$$\hat{R}_p^{-1} = R_p^{-1} + Y_{dl}, \tag{19}$$

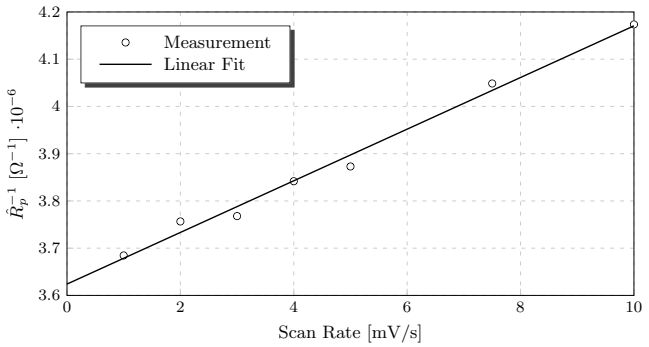

Figure 5. Plot of inverse polarization resistance vs. scan-rate for a μLPR sensor made from AA 7075-T6 submersed in tap water.

such that Y_{dl} is defined by the admittance,

$$Y_{dl} = \left(\frac{C_{dl}}{20\,\mathrm{mV}}\right)\frac{dE_a}{dt} \tag{20}$$

where dE_a/dt is the scan rate. An example of this relationship is provided in Figure 5. In this example $C_{dl}/20\,\mathrm{mV}$ and R_p^{-1} correspond to the slope and y-intercept; these values were computed as $5.466\times10^{-8}\,\Omega^{-1}\cdot\mathrm{s}/\mathrm{mV}$ and $3.624\times10^{-6}\,\Omega$, respectively. For a scan rate of $dE_a/dt = 7.7\,\mathrm{mV/s}$, Y_{dl} is computed as $4.209\times10^{-7}\,\Omega^{-1}$. Finally, for a given solution, $\hat{R}_p$ can be compensated by,

$$R_p = \frac{\hat{R}_p}{1 - Y_{dl}\hat{R}_p} \qquad \text{for} \qquad Y_{dl}R_p < 1. \tag{21}$$

4. Experiment

4.1. Setup

The experiment consisted of twenty-four (24) μLPR sensors and twelve (12) control coupons. The coupons and μLPR sensors were made from AA 7075-T6. Each coupon was placed next to a pair of μLPR sensors. Each sensor was held in place using a non-reactive polycarbonate clamp with a nylon fitting. All the sensors and coupons were mounted on an acrylic plexiglass base with the embedded hardware placed on the opposite side of the frame, shown in Figure 6. An electronic precision balance (Tree HRB-203) with a calibrated range of $0 - 200\,\mathrm{g}$ ($\pm 0.001\,\mathrm{g}$) was used to weigh the coupons before and after the experiment. Finally, a weathering chamber (Q-Lab QUV/spray) promoted corrosion on the coupons and μLPR sensors by applying a controlled stream of tap water for 10 seconds every five minutes.

4.2. Procedure

First, the surface of each coupon was cleaned using sandblasting. Then, each coupon was weighed using the analytical balance. The entire panel of coupons and μLPR sensors were placed in the weathering chamber for accelerated testing. The experiment ran for approximately 60 days. During the experiment, a set of coupons were periodically removed from the weathering chamber. Throughout the experiment, the SHM embedded hardware was logging $\hat{R}_p$ from each μLPR sensor. The sample rate was set at one sample per minute. Once accelerated testing was finished, the coupons were removed and the LPR data was downloaded and archived for analysis. The corrosion byproducts were removed from each coupon by applying micro-bead blasting to the coupon surface. Finally, the cleaned coupons were weighted using the analytical scale to compute the relative corrosion depth during the experiment. Figure 7 shows images of coupons before and after micro-bead blasting. Also shown are images comparing two sets of three coupons after 15 days and 57 days of corrosion proceeding micro-bead blasting.

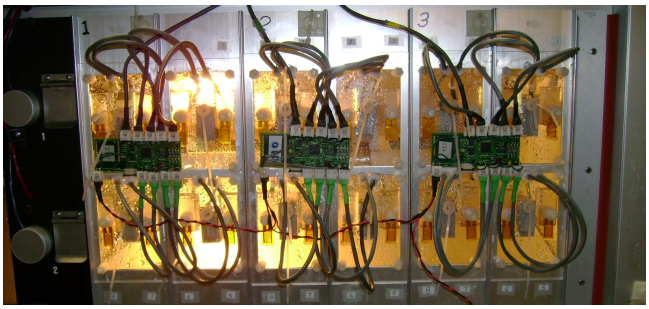

(a)

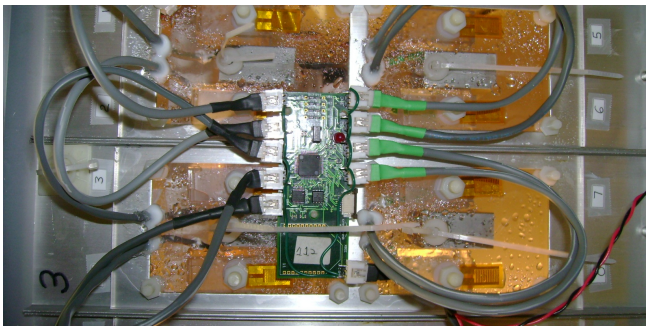

(b)

Figure 6. Experimental setup showing (a) all 24 μLPR sensors, 12 coupons and three AN101 instrumentation boards and (b) a close-up view of one of the panels used in the experiment.

5. Results

5.1. Coupon Corrosion

The corrosion byproducts were carefully removed using micro-bead blasting. The pitting depth, d, of each coupon was calculated using the formula,

$$d = \sqrt[3]{\frac{3m_{loss}}{2\pi\rho N_{pit}A_{exp}}}, \tag{22}$$

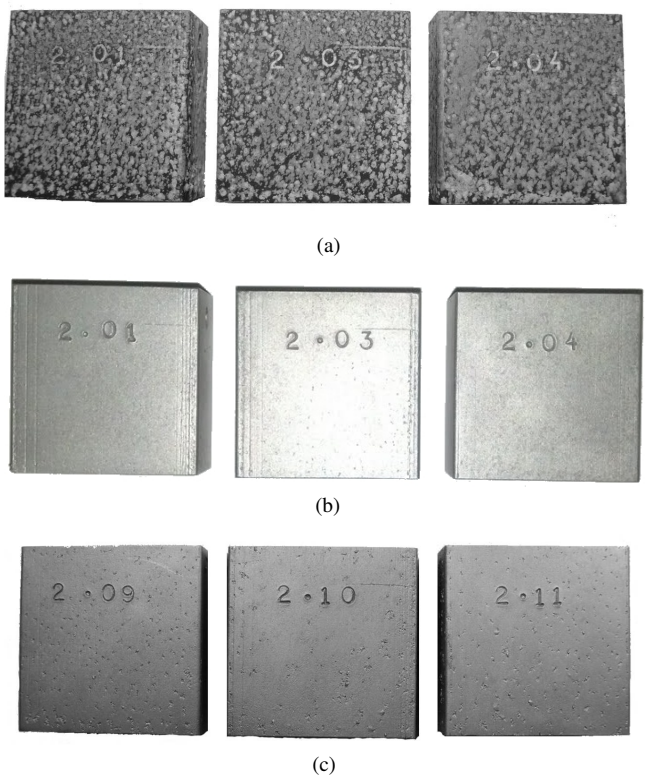

Figure 7. Image of the three AA 7075-T6 coupons (ID 2.01, 2.03 and 2.04) after approximately 15 days of corrosion testing showing (a) the condition of the coupons before cleaning and (b) after cleaning using micro-bead blasting. Also shown for comparison are (c) three AA 7075-T6 coupons (ID 2.09, 2.10 and 2.11) after 57 days and cleaning using micro-bead blasting.

where values for the mass loss m_{loss}, exposed surface area A_{exp}, resulting pit-depth, d, and total time of exposure of each coupon is provided in Table 1 in the Appendix. Values for the pitting density and ρ were set at $N_{pit} = 11\,\mathrm{cm}^{-2}$ and $\rho = 2.810\,\mathrm{g/cm^3}$, respectively. The pitting density was computed by counting the average number of pits over the surface for coupons 2.06 and 2.08. The measurement uncertainty in the pit-depth due to uncertainty in the mass loss, Δm_{loss} and pit density, ΔN_{pit}, is approximately,

$$\Delta d \approx \frac{d}{3}\left(\frac{\Delta m_{loss}}{m_{loss}} + \frac{\Delta N_{pit}}{N_{pit}}\right), \tag{23}$$

where $\Delta m_{loss} = \pm 0.001\,\mathrm{g}$ is the minimum resolution of the scale and $\Delta N_{pit} = \pm 3\,\mathrm{cm}^{-2}$ was the standard deviation of the measured pit density over $1\,\mathrm{cm}^2$ sample areas for coupons 2.06 and 2.08.

5.2. μLPR Corrosion

The linear polarization resistance measurements were used to compute corrosion pit-depth for each μLPR sensor. The computed pit-depth for each of the 24 μLPR sensors over a period of approximately 60 days is provided in Figure 2(a).

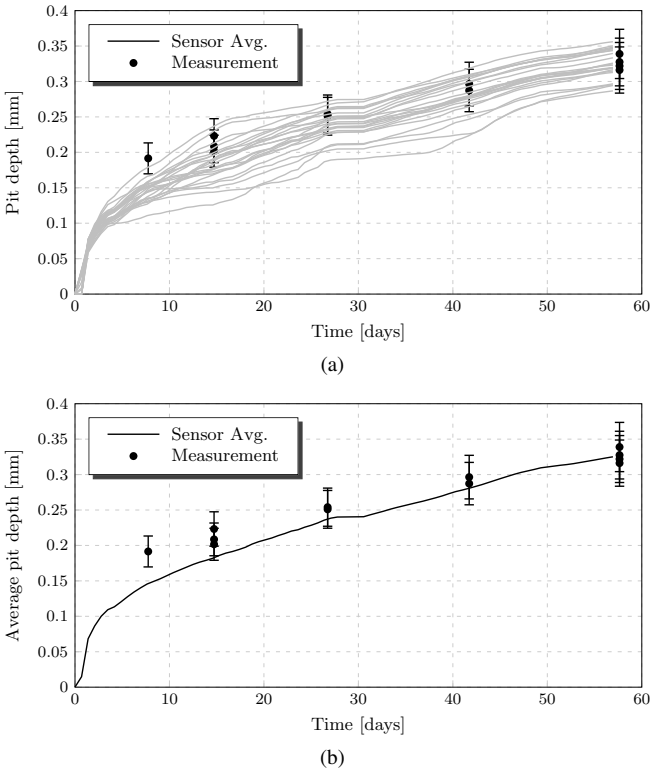

Figure 8. Comparison of the measured and computed pit-depth over a period of approximately 60 days for (a) each μLPR sensor and (b) the average of all μLPR sensors.

Superimposed in the plot are the pit-depth measurements of the corrosion coupons. The average computed pit-depth for each of the 24 μLPR sensors over the same period is shown in Figure 2(b).

Next, the corrosion coupons were used to evaluate the performance of the μLPR sensor. Figure 9(a) compares the measured pit-depth with the pit-depth computed from each of the 24 μLPR sensors during the removal of each corrosion coupon. A solid line is used to identify an ideal one-to-one relationship between the measured and computed pit-depth. Figure 9(b) shows the distribution of the computed residuals from Figure 9(a). The residuals follow a Gaussian distribution with a computed mean and standard deviation of $0.0153\,\mathrm{mm}$ and $0.0272\,\mathrm{mm}$, accordingly. Figure 9(c) compares the measured pit-depth with the pit-depth computed from the average of the 24 μLPR sensors during the removal of each corrosion coupon. Also provided in the plot are the error bars corresponding to one standard deviation in the corrosion measurements.

6. Applications in Prognostics

The data generated from this experiment can be used to demonstrate the feasibility of the μLPR sensor for use in prognostics. According to (Vachtsevanos, Lewis, Roemer, Hess, & Wu, 2006), prognostics is the ability to predict ac-

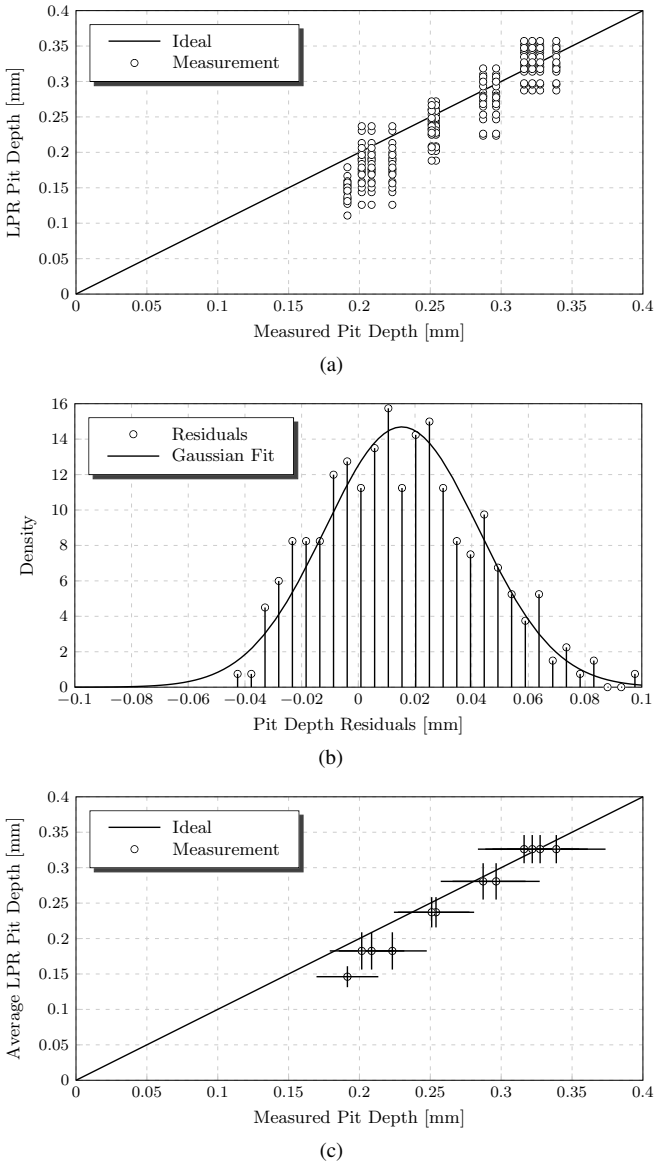

Figure 9. Direct comparison of the measured versus computed pit-depth for (a) each μLPR sensor measured at each coupon removal, (b) the corresponding distribution of the computed residuals and (c) average μLPR sensor measurement at each coupon removal.

curately and precisely the Remaining Useful Life (RUL) of a failing component or subsystem. In this application the failing component is the metallic structure being monitored, more specifically AA 7075-T6, by the μLPR sensor. The physical quantity to be predicted, otherwise referred to as the fault dimension, is the pit-depth of the metallic structure.

Typically the fault dimension is not a quantity that is directly measured. Rather, the fault dimension is commonly computed from a mapping of one or more indirect measures, or features. In this application, the features are temperature and polarization resistance. In this particular experiment, temperature remained at (or near) room temperature. As a result, the primary feature is polarization resistance. The fault dimension was computed using the mathematical model derived earlier in Section 2.4 as a mapping function.

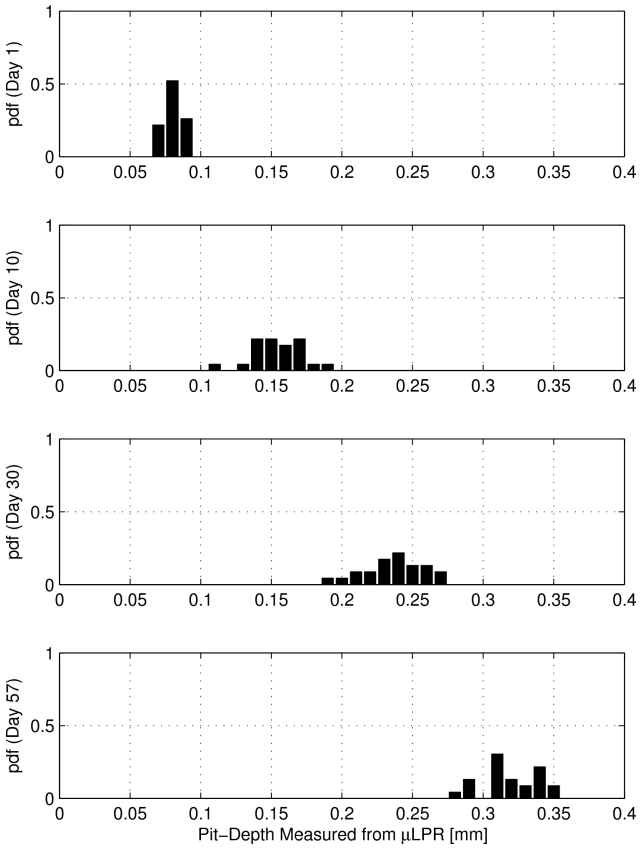

Figure 10. Histograms of the fault dimension (pit depth) after 1, 10, 30 and 57 days into the experiment.

Of course, the fault dimension does not stay constant with time. The fault grows with many factors including the current fault dimension and the operating environment. In this example, the operating environment is the environmental chamber with the 5 minute spray cycle operating at room temperature. Figure 10 shows the distribution of the fault dimension for 24 μLPR sensors at four different time intervals correspond to the end of day 1, 10, 30 and 57. As time progresses, the distribution of the fault dimension changes. In practice, a fault-growth model is used to project the fault dimension over a future time interval. The fault-growth model usually includes multiple factors. In this example, the fault-growth, or corrosion rate, is dependent on factors that include the solution, temperature, pH and time of wetness. Please note: in the scope of this paper no fault-growth model was studied. All of the data analysis for prognosis feasibility was performed a-posteriori using the μLPR data only.

Knowledge of the fault dimension distribution at any moment in time is important in prognostics. The RUL is defined as a projection of the fault dimension onto the time domain for a fixed value, referred to as the failure threshold. The fail-

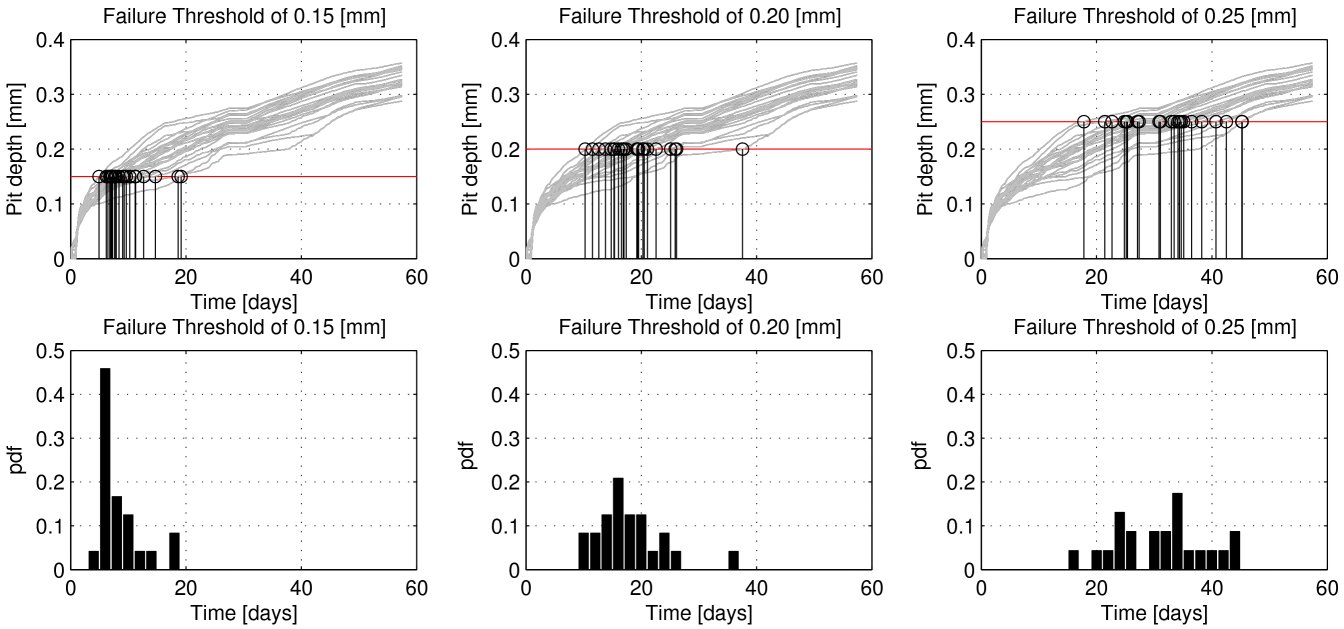

Figure 11. Prognosis feasibility demonstrated by (top) plots of (top) fault-dimension (pit-depth) vs. time identifying the time when fault-dimension computed from each of the 24 μLPR sensors first exceeds the failure threshold of (from left-to-right) $0.150\,\mathrm{mm}$, $0.200\,\mathrm{mm}$ and $0.250\,\mathrm{mm}$, respectively. Also shown (bottom) are histograms of the RUL corresponding to each respective failure threshold.

ure threshold value is usually determined a-priori by an engineer with experience in the particular area of application. In this example, three failure thresholds are selected for the fault dimension: $0.150\,\mathrm{mm}$, $0.200\,\mathrm{mm}$ and $0.250\,\mathrm{mm}$. The upper plots in Figure 11 show the fault-dimension measured from each μLPR sensor over a period of approximately 60 days. Starting from left to right, the failure threshold values of $0.150\,\mathrm{mm}$, $0.200\,\mathrm{mm}$ and $0.250\,\mathrm{mm}$ are identified with a red horizontal line. The intersection of the failure threshold and each of the 24 fault-dimension curves are identified with a superimposed stem plot. The lower plots in Figure 11 show the probability density function (pdf) of each respective stem plot on the time-axis. Each pdf represents the RUL starting from the beginning of the experiment at time zero. Note, as the failure threshold is raised, both the mean value and variance of the RUL grows. This demonstrates the uncertainty in the RUL prediction increases over an increasing time interval, which is to be expected.

7. Summary

A micro-sized LPR (μLPR) sensor was presented for corrosion monitoring in Structural Health Management (SHM) applications. An experimental test was performed to compare corrosion measurements from twenty-four μLPR sensors with twelve corrosion coupons. Both the corrosion coupons and sensors were constructed from the same material, AA 7075-T6. According to the results, the pit-depth computed from the μLPRsensors agreed the pit-depth measured from the corrosion coupons to within a statistical confidence of 95%. The results indicate multiple μLPR sensors can be used to provide an accurate measurement of corrosion. The paper concluded with a feasibility study for the μLPR sensor in prognostic applications.

Future work includes a combination of prognostic model development, extensive laboratory testing and field testing. Before the μLPR sensor can be used in prognostic applications, a prognostic algorithm, more specifically a fault-growth model, must be developed. Additional laboratory testing is required to: evaluate the μLPR sensors for different alloys (eg. AA 2024-T3); perform experiments using standardized protocols (eg. SAE J2334 & ASTM G85); perform a blind study evaluating μLPR-based prognostic algorithms; and certify the AN101 SHM system for electromagnetic interference (EMI), electromagnetic conductance (EMC) and environmental conditions following MIL-STD-461F and MIL-STD-810G specifications. Field testing is necessary to evaluate the performance of the sensor and SHM system in a real-world environment. The system has been certified for initial flight testing on a C-130 legacy aircraft. Follow-on testing includes performing a smaller-scale validation experiment for the μLPR in-flight.

Acknowledgment

All funding and development of the sensors and systems in the project has been part of the US government's SBIR programs. In particular: 1) In preparing the initial system design and development, funding was provided by the US Air Force under SBIR Phase II contract # F33615-01-C-5612 monitored

by Dr. James Mazza, 2) Funding for the development and experimental set-up was provided by the US Navy under SBIR Phase II contract # N68335-06-C-0317 monitored by Dr. Paul Kulowitch, and 3) for further improvements and scheduled field installations by the US Air Force under SBIR Phase II contract # FA8501-11-C-0012 monitored by Mr. Feraidoon Zahiri.

NOMENCLATURE

β_a	Anodic Tafel slope	V/dec
β_c	Cathodic Tafel slope	V/dec
ρ	Density	g/mm^3
d	Corrosion depth	cm
k	LPR sample index	–
i_{corr}	Corrosion current density	A/cm^2
i_{pit}	Pitting current density	A/cm^2
i_{pv}	Passive current density	A/cm^2
m_{loss}	Mass loss due to corrosion	g
z	Number of electrons lost per atom	–
Δd	Corrosion depth uncertainty	cm
Δm_{loss}	Mass loss uncertainty	g
ΔN_{pit}	Pit density uncertainty	cm^{-2}
A_{exp}	Exposed coupon area	cm^2
A_{sen}	Effective sensor area	cm^2
AW	Atomic Weight	g/mol
B	Proportionality constant	V/dec
C_{dl}	Double-layer capacitance	F
E_a	Applied potential	V
E_{corr}	Corrosion voltage	V
EW	Equivalent weight	g/mol
F	Faraday's constant	C/mol
I_a	Applied current	A
I_{corr}	Corrosion current	A
I_{dl}	Scanning current from C_{dl}	A
M	Number of moles reacting	mol
N	Total number of μLPR samples	–
N_{pit}	Pit density	cm^{-2}
Q_{corr}	Charge from oxidation reaction	C
R_p	Polarization resistance	Ω
$\hat{R}_p$	Measured polarization resistance	Ω
R_s	Solution resistance	Ω
T_s	Sampling period	s
Y_{dl}	Scanning admittance from C_{dl}	s

REFERENCES

Bockris, J. O., Reddy, A. K. N., & Gambola-Aldeco, M. (2000). *Modern Electrochemistry 2A. Fundamentals of Electrodics* (2nd ed.). New York: Kluwer Academic/Plenum Publishers.

Buchheit, R. G., Hinkebein, T., Maestas, L., & Montes, L. (1998, March 22-27). Corrosion Monitoring of Concrete-Lined Brine Service Pipelines Using AC and DC Electrochemical Methods. In *CORROSION 98.* San Diego, Ca.

Burstein, G. T. (2005, December). A Century of Tafel's Equation: 1905-2005. *Corrosion Science*, *47*(12), 2858-2870.

G102, A. S. (1994). Standard Practice for Calculation of Corrosion Rates and Related Information from Electrochemical Measurements. *Annual Book of ASTM Standards*, *03.02*.

G59, A. S. (1994). Standard Practice for Conducting Potentiodynamic Polarization Resistance Measurements. *Annual Book of ASTM Standards*, *03.02*.

Harris, S. J., Mishon, M., & Hebbron, M. (2006, October). Corrosion Sensors to Reduce Aircraft Maintenance. In *RTO AVT-144 Workshop on Enhanced Aircraft Platform Availability Through Advanced Maintenance Concepts and Technologies.* Vilnius, Lithuania.

Huston, D. (2010). *Structural Sensing, Health Monitoring, and Performance Evaluation* (B. Jones & W. B. S. J. Jnr., Eds.). Taylor and Francis.

Introduction to Corrosion Monitoring. (2012, August 20). Online. Available from `http://www.alspi.com/introduction.htm`

Twomey, M. (1997). Inspection Techniques for Detecting Corrosion Under Insulation. *Material Evaluation*, *55*(2), 129-133.

Vachtsevanos, G., Lewis, F., Roemer, M., Hess, A., & Wu, B. (2006). *Intelligent Fault Diagnosis and Prognosis for Engineering Systems*. Hoboken, NJ, USA: John Wiley and Sons.

Wagner, C., & Traud, W. (1938). *Elektrochem*, *44*, 391.

BIOGRAPHIES

Douglas W. Brown is the senior systems engineer at Analatom with eight years of experience developing and maturing PHM and fault-tolerant control systems in avionics applications. He received the B.S. degree in electrical engineering from the Rochester Institute of Technology in 2006 and the M.S/Ph.D. degrees in electrical engineering from the Georgia Institute of Technology in 2008 and 2011, respectively. Dr. Brown is a recipient of the National Defense Science and Engineering Graduate Fellowship and has received several best-paper awards in his work in prognostics and fault-tolerant control.

Duane Darr is the senior embedded hardware engineer at Analatom with over 30 years of experience in the software and firmware engineering fields. He completed his undergraduate work in physics, and graduate work in electrical engineering and computer science at Santa Clara University. Mr. Darr's previous work at Epson Imaging Technology Center, San Jose, California, as Senior Software Engineer,

Data Technology Corporation, San Jose, California as Senior Firmware Engineer, and Qume Inc., San Jose California, as Member of Engineering Staff/Senior Firmware Engineer, focused on generation and refinement of software and firmware solutions for imaging core technologies as well as digital servo controller research, development, and commercialization.

Jefferey Morse is the director of advanced technology at Analatom since 2007. Prior to this, he was a senior scientist in the Center for Micro and Nano Technology at Lawrence Livermore National Laboratory. He received the B.S. and M.S. degrees in electrical engineering from the University of Massachusetts Amherst in 1983 and 1985, respectively, and a Ph.D. in electrical engineering from Stanford University in 1992. Dr. Morse has over 40 publications, including 12 journal papers, and 15 patents in the areas of advanced materials, nanofabrication, sensors and energy conversion technologies. He has managed numerous projects in various multidisciplinary technical areas, including electrochemical sensors and power sources, vacuum devices, and microfluidic systems.

Bernard Laskowski is the president and senior research scientist at Analatom since 1981. He received the Licentiaat and Ph.D. degrees in Physics from the University of Brussels in 1969 and 1974, respectively. Dr. Laskowski has published over 30 papers in international refereed journals in the fields of micro physics and micro chemistry. As president of Analatom, Dr. Laskowski managed 93 university, government, and private industry contracts, receiving a U.S. Small Business Administration Administrator's Award for Excellence.

Table 1. Experimental measurements of coupon corrosion.

Coupon ID	Time Exposed $[\mathrm{min}]$	Area $[\mathrm{cm}^2]$	Initial Mass [g]	Final Mass [g]	Mass Loss [g]	pit-depth $[\mathrm{mm}]$
Control	0	5.801×10^1	7.6870×10^1	7.6869×10^1	1×10^{-3}	N/A
2.01	2.1198×10^4	5.805×10^1	7.7253×10^1	7.7215×10^1	3.8×10^{-2}	2.232×10^{-1}
2.02	1.1160×10^4	5.798×10^1	7.6842×10^1	7.6818×10^1	2.4×10^{-2}	1.915×10^{-1}
2.03	2.1198×10^4	5.799×10^1	7.6927×10^1	7.6896×10^1	3.1×10^{-2}	2.068×10^{-1}
2.04	2.1198×10^4	5.805×10^1	7.6897×10^1	7.6869×10^1	2.8×10^{-2}	2.016×10^{-1}
2.05	6.0090×10^4	5.801×10^1	7.6967×10^1	7.6886×10^1	8.1×10^{-2}	2.873×10^{-1}
2.06	3.8510×10^4	5.798×10^1	7.6884×10^1	7.6828×10^1	5.6×10^{-2}	2.540×10^{-1}
2.07	6.0090×10^4	5.800×10^1	7.6945×10^1	7.6856×10^1	8.9×10^{-2}	2.964×10^{-1}
2.08	3.8510×10^4	5.803×10^1	7.6921×10^1	7.6810×10^1	5.4×10^{-2}	2.509×10^{-1}
2.09	8.3010×10^4	5.802×10^1	7.7005×10^1	7.6885×10^1	1.20×10^{-1}	3.275×10^{-1}
2.10	8.3010×10^4	5.802×10^1	7.7165×10^1	7.7057×10^1	1.08×10^{-1}	3.162×10^{-1}
2.11	8.3010×10^4	5.802×10^1	7.6865×10^1	7.6751×10^1	1.14×10^{-1}	3.219×10^{-1}
2.12	8.3010×10^4	5.802×10^1	7.6902×10^1	7.6769×10^1	1.33×10^{-1}	3.389×10^{-1}